Magnetic structures of PrMn₇O₁₂: Intersublattice magnetoelastic coupling and incommensurate spin canting

Dylan Behr,[1,*] Ran Liu,[2,3,†] Kazunari Yamaura ⬤,[2,3] Alexei A. Belik ⬤,[2] Dmitry D. Khalyavin,[4] and Roger D. Johnson ⬤[1,5]

[1]*Department of Physics and Astronomy, University College London, Gower Street, London WC1E 6BT, United Kingdom*

[2]*Research Center for Materials Nanoarchitectonics (MANA), National Institute for Materials Science (NIMS),*
1-1 Namiki, Tsukuba, Ibaraki 305-0044, Japan

[3]*Graduate School of Chemical Sciences and Engineering, Hokkaido University, North 10 West 8, Kita-ku,*
Sapporo, Hokkaido 060-0810, Japan

[4]*ISIS facility, Rutherford Appleton Laboratory-STFC, Chilton, Didcot OX11 0QX, United Kingdom*

[5]*London Centre for Nanotechnology, University College London, London WC1E 6BT, United Kingdom*

We report on the magnetic structures of PrMn₇O₁₂, resolving both a high-temperature structure in common with the other R^{3+}Mn₇O₁₂ systems and an additional low-temperature phase characterized by a superposed incommensurate (ICM) spin canting. A phenomenological model is developed to account for large magnetoelastic coupling immediately below the Curie temperature, demonstrating that $A'B$ exchange is primarily responsible for the ferrimagnetic structures observed across the R^{3+}Mn₇O₁₂ family. Finally, an analytical mean-field minimal model is presented that successfully accounts for all magnetic structures observed in this family of materials, including the canted commensurate and ICM ground states.

I. INTRODUCTION

The ABO₃ (B = Mn) perovskite manganites have undergone intensive study since the late 1940s, a period during which research was spurred on by successive milestones of synthesis and theoretical and experimental discovery [1,2]. These include the observation of metal-insulator transitions [1], colossal magnetoresistance [3], multiferroic and magnetodielectric behavior [4], as well as demonstration of functionality as catalysts [5], electrolytes [6], and thermoelectric ceramics and sensors [7]. Their structural and chemical flexibility underpins their diverse physical properties, making them canonical systems for the study of structure-property relationships in strongly correlated electron systems.

Owing to their high-pressure and high-temperature synthesis requirements, the AA'_3B_4O₁₂ (A' = Mn, B = Mn) quadruple perovskite manganites (QPMs) are relatively less well studied, and significant ambiguities still exist in the characterization of their structural, electronic, and magnetic features [8,9]. Derived from their simple perovskite ABO₃ analogs, QPMs are distinguished by a chemical ordering where three out of four A-site cations (here labeled A') are replaced by Mn, stabilized by a pattern of large octahedral tilts ($a^+a^+a^+$ in Glazer notation) [10,11]. The resulting aristotypical structure has cubic $Im\bar{3}$ symmetry and hosts two distinct sublattices of magnetic Mn cations (A' and B). The various structures exhibited in QPMs are strongly influenced by the choice of A-site cation: The A-site valence determines the proportion of Mn³⁺ : Mn⁴⁺ on B sites, which in turn determines the ratio of Jahn-Teller (JT) active octahedral MnO₆ units to non-JT-active units [9,12–16]. Here, A^{3+} cations permit homovalent Mn³⁺ ions at all B sites, which typically stabilize monoclinic $I2/m$ crystal structures at room temperature [17,18] due to orbital order analogous to that observed in LaMnO₃, where MnO₆ octahedra are alternately elongated along approximately **a** and **c** in the ac plane, indicating a checkerboard arrangement of half-occupied $d_{3x^2-r^2}$ and $d_{3z^2-r^2}$ orbitals of the Mn³⁺ $3d^4$ B-site cations [19–21].

Based upon the Goodenough-Kanamori-Anderson (GKA) [2,22,23] rules taken in the limit of 180° Mn-O-Mn bond angles, the orbital order is expected to stabilize an A-type antiferromagnetic (AFM) structure on the B sites, with ferromagnetic (FM) exchange between half-filled and empty e_g orbitals oriented within the ac plane and AFM exchange between empty e_g B-site orbitals separated along **b**. However, complicating this network of B-site magnetic exchange is the presence of (i) the additional magnetic A'-site sublattice of Mn³⁺ ions and (ii) the pattern of large octahedral tilts. The former extends the total set of exchange interactions present, introducing $A'B$ and AA' nearest-neighbor exchange, which may compete with and frustrate BB exchanges and one another. The latter can modulate the strength of competing exchange pathways between magnetic ions, which depend strongly on M-O-M bond angles.

---

*Contact author: dylan.behr.20@ucl.ac.uk

†Present address: Institute of Scientific and Industrial Research, Osaka University, Mihogaoka 8-1, Ibaraki, Osaka 567-0047, Japan.

Authors of previous studies on the $R^{3+}Mn_7O_{12}$ systems have identified a Γ-point ferrimagnetic (FIM) phase common to all trivalent-R quadruple perovskites, comprising a C-type AFM structure on B sites (AFM planes staked FM) and a C-type-derived FIM structure on A' sites which order concomitantly on cooling through the magnetic transition temperature T_1 [24]. Indeed, these magnetic structures are observed across $R =$ La, Ce, Nd, Sm, and Eu QPMs, with magnetic transition temperatures of $T_1 = 79.5$, 80, 83, 85, 87, and 87 K, respectively, increasing with decreasing ionic radius. Furthermore, trivalent-A QPMs $BiMn_7O_{12}$, $DyMn_7O_{12}$, and YMn_7O_{12} exhibit the same or similar FIM modes as their aforementioned family members, albeit with additional exotic magnetic and structural phenomena: $BiMn_7O_{12}$ hosts additional magnetic modes, including a polar AFM E-type order that couples to a polar distortion of the crystal structure [25], while YMn_7O_{12} and $DyMn_7O_{12}$ exhibit emergent dipolar glass transitions that, in the case of $DyMn_7O_{12}$, couple to the magnetic order parameter [26,27].

In $R^{3+}Mn_7O_{12}$ compounds with a larger rare-earth ion, namely, $R =$ La and Nd, a further magnetic transition is observed on cooling below $T_2 = 22.5$ and 12 K associated with the onset of superposed orthogonal modes on B sites, with propagation vectors $(0,1,0)$ and $(k_x, 1, k_z)$, respectively. In $LaMn_7O_{12}$, the additional magnetic mode resembles commensurate (CM) A-type AFM order, with AFM spin correlations between nearest-neighbor B sites along **b** and FM correlations along **a** and **c**. The additional magnetic mode in $NdMn_7O_{12}$ is similar, augmented by an incommensurate (ICM) modulation within the ac plane. In $BiMn_7O_{12}$, which also hosts a large A-site cation, a further magnetic mode with propagation vector $(0,1,0)$ is also observed below $T_3 = 27$ K, although details of the associated magnetic structure have not yet been determined. Whether CM or ICM with the nuclear lattice, these superposed magnetic modes manifest as spin canting of the higher-temperature FIM magnetic structures, resulting in highly noncollinear ground states.

The apparently universal behavior below T_1, contrasted with the exotic noncollinear CM or ICM ground states found only in certain compositions below T_2, demands a general model of magnetism in the QPMs that outlines the responsible set of interactions for the observed structures and trends. Herein, we make progress toward this aim through the study of $PrMn_7O_{12}$, an as yet relatively understudied member of the $R^{3+}Mn_7O_{12}$ family. $PrMn_7O_{12}$ has been reported to crystallize in both trigonal ($R\bar{3}$) and monoclinic ($I2/m$) polymorphs [28]. The monoclinic polymorph, pertinent to this paper, has been observed from DC-susceptibility measurements to undergo a magnetic transition at T_1 concomitant with the development of a net macroscopic magnetization. However, to our knowledge, no microscopic study of magnetism has yet been performed on the system. In this paper, we report on the magnetic structures of monoclinic $PrMn_7O_{12}$ based on neutron powder diffraction (NPD) experiments, and we evidence strong magnetoelastic coupling in the system. A phenomenological theory of the magnetoelastic coupling is formulated which is then mapped onto the microscopic degrees of freedom present. Our observations and analyses are used to inform a general model of magnetism in the QPM family, accounting for the presence of pure Γ-point FIM, CM, and ICM canted

ground states, outlining the competing instabilities responsible. The paper is organized as follows: In Sec. II, we briefly describe the experimental methods; in Sec. III, we present our experimental results from which the magnetic phases of $PrMn_7O_{12}$ are characterized; and in Sec. IV, we present a phenomenological model for intersublattice magnetoelastic coupling and comment on the wider magnetic phase diagram for the RMn_7O_{12} family derived from an empirically constrained minimal mean-field Heisenberg model presented in Appendix B. Finally, we summarize our conclusions in Sec. V.

II. EXPERIMENT

Polycrystalline $PrMn_7O_{12}$ samples were prepared from stoichiometric mixtures of Mn_2O_3, Mn_3O_4, and Pr_6O_{11}. The mixture was placed in four Pt capsules and treated at 6 GPa and ~ 1600 K for 2 h (heating time to the synthesis temperature was 10 min) in a belt-type high-pressure apparatus. After the heat treatments, the samples were quenched to room temperature, and the pressure was slowly released. All obtained samples were black pellets. Magnetic susceptibility measurements were performed on a Quantum Design magnetic property measurement system (MPMS-3) between 2 and 100 K in a 100 Oe field under both zero-field-cooled (ZFC) and field-cooled-on-cooling (FCC) conditions. A magnet-reset procedure was applied before the ZFC measurement. Isothermal magnetization measurements were performed between -70 and 70 kOe at 5, 25, and 60 K. Heat capacity measurements were made in 0 and 90 kOe fields using a Quantum Design physical property measurement system (PPMS). NPD measurements were performed on the WISH time-of-flight diffractometer [29] at ISIS, the UK neutron and muon spallation source. The sample (~ 0.65 g) was lightly packed into a thin 3-mm-diameter cylindrical vanadium can and mounted within a ^{4}He cryostat. Data were collected with high counting statistics at a fixed temperature within each magnetic phase, including the paramagnetic phase for reference. Data were also collected with lower counting statistics on warming in the temperature range 1.5–300 K to ascertain thermal trends in crystal structure and magnetic order. All diffraction data were refined using FULLPROF [30]. Symmetry analyses were performed using the ISOTROPY software suite, particularly the ISODISTORT tool for modal decomposition of nuclear structures and identification of magnetic normal modes, and the ISOTROPY interactive command line tool for the systematic derivation of invariants [31,32].

III. RESULTS

Specific heat capacity [Fig. 1(a)] and magnetic susceptibility [Fig. 1(b)] measurements indicate the presence of two magnetic transitions at $T_1 = 82$ K and $T_2 = 12$ K, the first of which coincides with the development of a bulk magnetic moment [Fig. 1(b)]. Indeed, a significant remnant magnetization was measured in isothermal field-dependent magnetization measurements at 60, 25, and 5 K, consistent with long-range (FM) FIM order (see Fig. 1 inset). Both specific heat anomalies shift to higher temperature in an applied field, with the lower-temperature feature becoming sharper and the
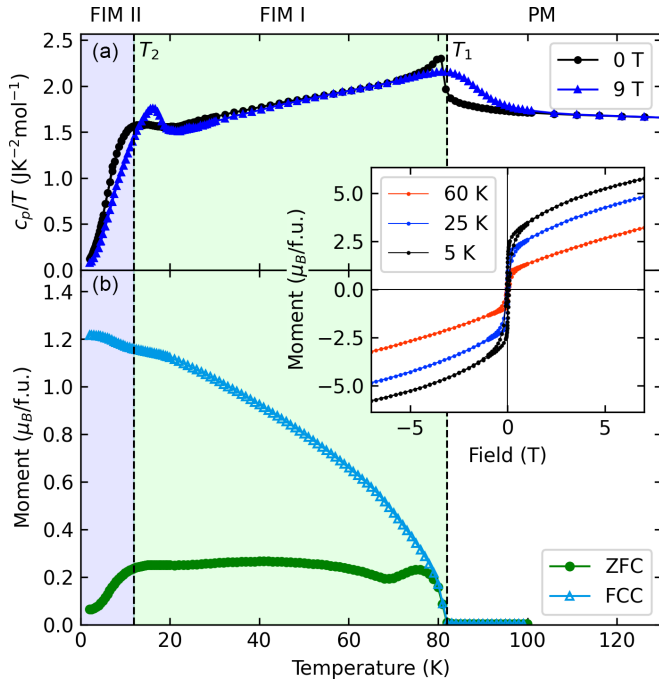
FIG. 1. (a) Specific heat capacity over temperature of PrMn$_7$O$_{12}$ in zero applied field and 9 T. Magnetic transitions inferred from anomalous features in the heat capacity are indicated by vertical dashed lines. (b) Zero-field-cooled (ZFC) and field-cooled-on-cooling (FCC) magnetization measurements of polycrystalline PrMn$_7$O$_{12}$ under an applied DC field of 100 Oe. The inset depicts isothermal moment vs field measurements at temperatures 5, 25, and 60 K.

higher-temperature feature becoming broader. The origin of this behavior is not clear, but the observed changes at T_1 are consistent with the field coupling to the net magnetization.

NPD data collected with high counting statistics at 100 K within the paramagnetic phase of PrMn$_7$O$_{12}$ were used to refine a structural model based on the published $I2/m$ phase [28], with excellent agreement achieved [see Fig. 2(a)]. The structural parameters are detailed in Table I. No significant impurities were found in the sample, with all nuclear

TABLE I. Crystal structure parameters of PrMn$_7$O$_{12}$ (space group $I2/m$) refined at 100 K. The lattice parameters were determined to be $a = 7.49813(7)$ Å, $b = 7.34352(6)$ Å, $c = 7.49291(7)$ Å, and $\beta = 91.2485(8)°$. Atomic Wyckoff positions are Pr: 2a [0,0,0]; Mn1: 2d [$\frac{1}{2}$, $\frac{1}{2}$, 0]; Mn2: 2c [$\frac{1}{2}$, 0, 0]; Mn3: 2b [0, $\frac{1}{2}$, 0]; Mn4: 4f [$\frac{3}{4}$, $\frac{3}{4}$, $\frac{1}{4}$]; Mn5: 4e [$\frac{3}{4}$, $\frac{3}{4}$, $\frac{3}{4}$]; O1,O4: 8j [x, y, z]; O2,O3: 4i [$x, 0, z$]. U_{iso} values were constrained to be the same for all Mn and all O, respectively. They were, Pr: 0.2(1); Mn: 0.6(4); O: 0.7(2) in units $\times 10^{-2}$ Å^2. The Pr site was occupied by 91% Pr, 9% Mn.

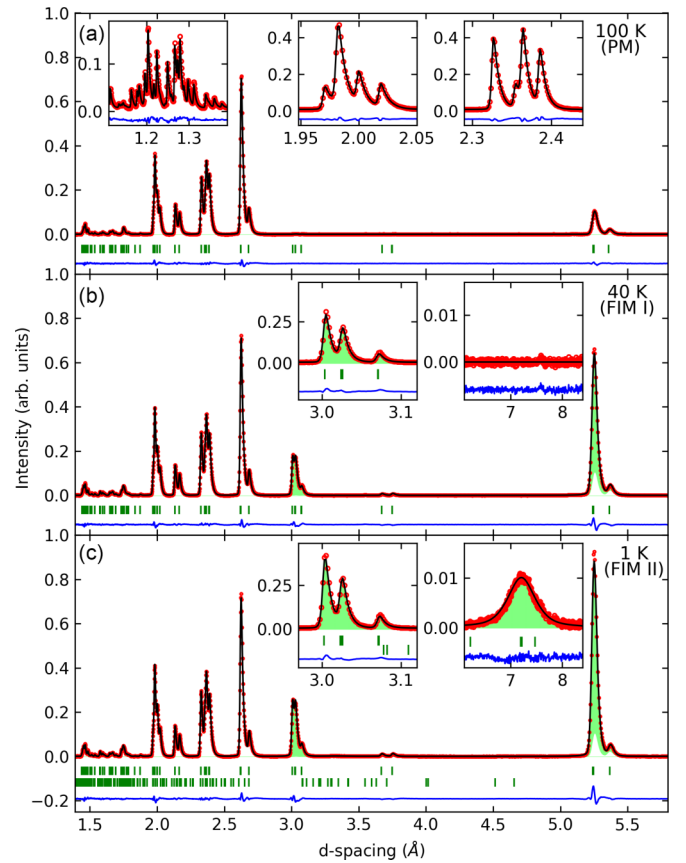| Atom	x	y	z
O1	0.9851(3)	0.6906(3)	0.8272(3)
O2	0.8210(4)	–	0.3125(4)
O3	0.1673(3)	–	0.3073(3)
O4	0.6890(2)	0.8252(3)	0.0130(2)

FIG. 2. Neutron powder diffraction patterns with Rietveld refined models in the (a) paramagnetic, (b) FIM I, and (c) FIM II phases. The observed intensity pattern is depicted with red points while the calculated intensity is overlaid in black. Magnetic intensities appearing below T_1 and T_2 are filled in lime green. Green ticks below indicate the calculated positions of reflections originating from the nuclear structure and Γ-point magnetic order (upper row), and incommensurate (ICM) order with propagation vector (k_x, 1, k_z) (lower row). All inset plots of (a) and the left-hand insets of (b) and (c) depict the fitting of selected peaks from a high-resolution detector bank, while those depicted to the right in plots (b) and (c) highlight a selected region of the main plots $\sim$7.1 Å.

peaks being accounted for by the $I2/m$ model. It is worth stressing that the $R\bar{3}$ is absent from our sample. Refinements indicate A sites are partially occupied by Mn, with Mn accounting for $\sim$10% and Pr the remaining 90%.

Below T_1, additional magnetic intensities appeared at positions of allowed nuclear intensity, unambiguously indexing at $\mathbf{k}_\chi = (0, 0, 0)$ [see Fig. 2(b)]. Informed by the results of prior analyses on isostructural RMn$_7$O$_{12}$ systems [24], a magnetic structure transforming as the $m\Gamma_2^+$ irreducible representation (irrep) of the paramagnetic $I2/m$ parent was found to faithfully reproduce the observed magnetic intensities (see Fig. 3). Here, B sites order with a C$_b$-type AFM structure where nearest-neighbor spins separated along $\mathbf{b}$ are coaligned, while those along $\mathbf{a}$ and $\mathbf{c}$ are antialigned. Here, A' sites are found to order simultaneously with a FIM mode derived from a C$_a$-type structure, whereby nearest-neighbor spins separated along $\mathbf{a}$ are coaligned, while those along $\mathbf{b}$ and $\mathbf{c}$ are antialigned. The moments on A' and B sublattices are collinear with one
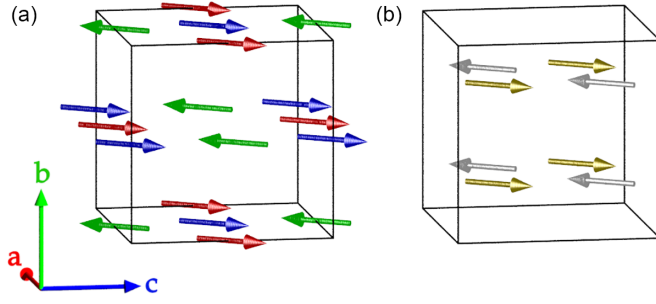
FIG. 3. The refined magnetic structure of $PrMn_7O_{12}$ in the FIM I phase at 40 K. The A' sublattice is presented in (a) with sites Mn1, Mn2, and Mn3 in red, green, and blue, respectively, while the B sublattice is presented in (b) with sites Mn4 and Mn5 in silver and gold, respectively.

another and lie within the ac plane. No ordered moments were found on the Pr A site. That the modes on both Mn sublattices transform as the same irrep of the $I2/m$ parent permits their cross-coupling and simultaneous ordering. We hereafter refer to the A'- and B-site modes as χ_a and χ_b, respectively (see Tables II and III for the definition of magnetic modes). The corresponding phase has one uncompensated Mn A'-site moment per formula unit and is labeled FIM I, which well accounts for the observed net magnetization (see Table IV for details).

On cooling below T_2 the Γ-point magnetic intensities continue to grow monotonically, while a new broad magnetic intensity appears in the vicinity of ~ 7.1 Å that indexes with the propagation vector $\mathbf{k}_\alpha = (0.207(6), 1, -0.03(2))$ [see Fig. 2(c)]. Systematic testing of candidate structures at the indexed propagation vector demonstrates that the diffraction pattern is well fit by an additional ICM AFM mode on the B sites that resembles an A_b-type structure in the $\mathbf{k} = (0, 1, 0)$ CM limit (nearest neighbors separated along $\mathbf{b}$ are antialigned, while those along $\mathbf{a}$ and $\mathbf{c}$ are aligned), augmented

TABLE II. $\mathbf{k} = (0, 0, 0)$ magnetic modes of $PrMn_7O_{12}$ defined in terms of relative mode amplitudes m of magnetic sites in the $y = 0$ (A' sites) and $y = \frac{1}{4}$ (B sites) planes of the unit cell. Sites related by I-centering have the same phase as per the propagation vector. Subscripts differentiate between the unique directions of χ AFM modes, while superscript i denotes any associated moment directions in a Cartesian basis coincident with the parent cubic axes.

| A' site | Frac. coords. | | | Mag. modes | | | |
	x	y	z	$F^i(A')$	$\chi_a^i(A')$	$\chi_b^i(A')$	$\chi_c^i(A')$
Mn1	0	0	$\frac{1}{2}$	$+m$	$+m$	$+m$	$-m$
Mn2	$\frac{1}{2}$	0	0	$+m$	$-m$	$+m$	$+m$
Mn3	$\frac{1}{2}$	0	$\frac{1}{2}$	$+m$	$+m$	$-m$	$+m$
B site				$F^i(B)$	$\chi_a^i(B)$	$\chi_b^i(B)$	$\chi_c^i(B)$
Mn4$_1$	$\frac{1}{4}$	$\frac{1}{4}$	$\frac{3}{4}$	$+m$	$+m$	$+m$	$+m$
Mn5$_1$	$\frac{1}{4}$	$\frac{1}{4}$	$\frac{1}{4}$	$+m$	$-m$	$-m$	$+m$
Mn4$_2$	$\frac{3}{4}$	$\frac{1}{4}$	$\frac{1}{4}$	$+m$	$-m$	$+m$	$-m$
Mn5$_2$	$\frac{3}{4}$	$\frac{1}{4}$	$\frac{3}{4}$	$+m$	$+m$	$-m$	$-m$

TABLE III. $\mathbf{k} = (k_x, 1, k_z)$ B-site magnetic modes of $PrMn_7O_{12}$ defined in terms of relative mode amplitudes m of magnetic sites in the $y = \frac{1}{4}$ plane of a unit cell at lattice site $\mathbf{R}$. The site phases are modulated by the propagation vector as follows: $m_{4_1} = m[\exp(i\mathbf{k} \cdot \mathbf{R})]$; $m_{5_1} = m[\exp(-ik_z/2)\exp(i\mathbf{k} \cdot \mathbf{R})]$; $m_{4_2} = m[\exp(-i(k_x + k_z)/2)\exp(i\mathbf{k} \cdot \mathbf{R})]$; $m_{5_2} = m[\exp(-ik_x/2)\exp(i\mathbf{k} \cdot \mathbf{R})]$. Partner sites in the adjacent plane at $y = \frac{3}{4}$ here are π out-of-phase with corresponding sites below as per the propagation vector. Notation and fractional coordinates are as given in Table II, with subscripts differentiating between the unique directions of α AFM modes.

| B sites | Mag. modes | | | |
	$\gamma^i(B)$	$\alpha_a^i(B)$	$\alpha_b^i(B)$	$\alpha_c^i(B)$
Mn4$_1$	$+m_{4_1}$	$+m_{4_1}$	$+m_{4_1}$	$+m_{4_1}$
Mn5$_1$	$-m_{5_1}$	$+m_{5_1}$	$+m_{5_1}$	$-m_{5_1}$
Mn4$_2$	$+m_{4_1}$	$-m_{4_2}$	$+m_{4_2}$	$-m_{4_2}$
Mn5$_2$	$-m_{5_2}$	$-m_{5_2}$	$+m_{5_2}$	$+m_{5_2}$

by a long wavelength modulation. Following the formalism of prior works, we label this mode α_b [24]. In refinements, a best minimal model is achieved when the moments associated with this mode are constrained to the ac plane in a direction perpendicular to the preexisting χ_b mode. In this case, the additional α_b magnetic component corresponds to a planar rocking of B-site moments about the average FIM I structure. However, our data analysis could not exclude a conical rotation of the spins about the FIM I structure (the same ambiguity was reported for the Nd system [24]). Indeed, it is typical for NPD that spin density waves or helicoidal modulations cannot readily be distinguished. The resulting canted magnetic structure is labeled FIM II, as shown in Fig. 4.

The crystal and magnetic structures were refined against variable-temperature NPD data to establish the evolution of structural and magnetic properties. In Fig. 5(a), the monoclinic lattice parameter β is plotted against temperature,

TABLE IV. Magnetic structure parameters refined in the FIM I and FIM II phases of $PrMn_7O_{12}$. Moment directions are given in spherical coordinates defined such that $m_z = m\cos(\theta) \parallel \mathbf{c}$, $m_x = m\cos(\phi)\sin(\theta) \parallel \mathbf{a}^*$, and $m_y = m\sin(\phi)\sin(\theta) \parallel \mathbf{b}$, with ϕ fixed to 0 to constrain moments to the ac plane. Here, $\mathbf{m} = [m_x, m_y, m_z]$ is the polarization of the respective magnetic modes χ_a, χ_b, and α_b, which are defined in terms of relative mode amplitudes m in Tables II and III.

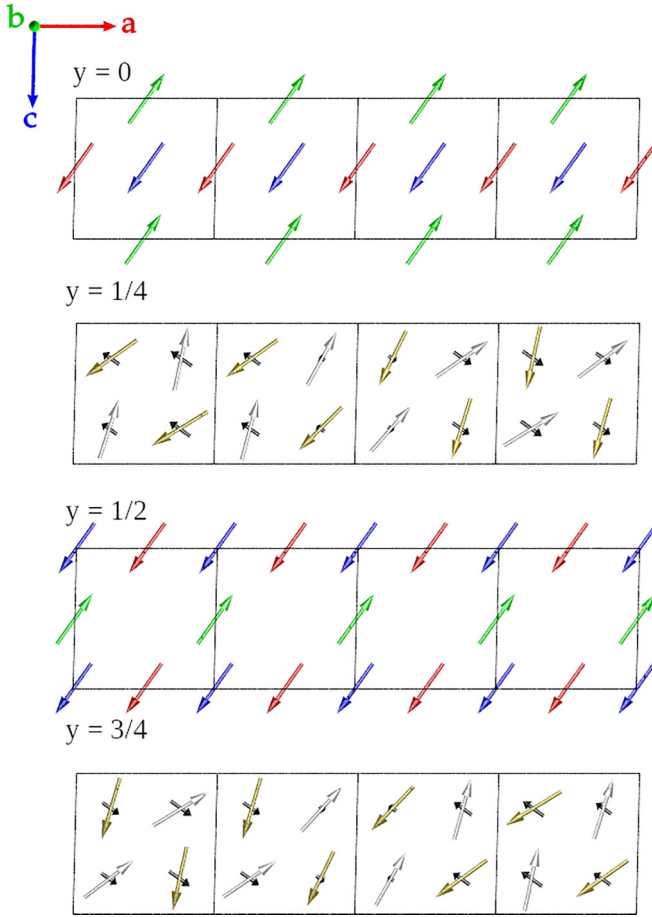| T (K) | 40 K | 1.5 K | |
Mn1	χ_a	χ_a	
m (μ_B)	2.80(1)	3.33(1)	
θ (°)	145.9(2)	144.6(1)	
Mn4	χ_b	χ_b	α_b
m (μ_B)	2.71(1)	3.22(1)	1.46(3)
θ (°)	145.9(2)	144.6(1)	54.6(1)
R (%)	3.74	3.92	
wR (%)	3.72	4.17	
R_{Mag} (%)	0.97	2.23	7.82

FIG. 4. The refined magnetic structure of PrMn$_7$O$_{12}$ in the FIM II phase at 1.5 K projected along **b**, presented in planes of constant y as indicated and spanning 4 unit cells along **a**. The A' sublattice is presented with sites Mn1, Mn2, and Mn3 in red, green, and blue, respectively, while the B sublattice is presented with sites Mn4 and Mn5 in silver and gold, respectively. The incommensurate α_b modulation is depicted here with thin black arrows superposed on the B-site moments, which rock about their average C_b structure.

with magnetic transitions indicated. Remarkably, a significant anomalous increase in the monoclinic angle is exhibited on cooling below T_1, which had otherwise increased with a shallow linear gradient on cooling through the paramagnetic phase (depicted in Fig. 5(a) with the red dashed line). We define the magnetostrictive component of β as the deviation of β from its linear trend in the paramagnetic state. It should be noted that PrMn$_7$O$_{12}$ is not unique in exhibiting such anomalous behavior of β at T_1, with LaMn$_7$O$_{12}$ and BiMn$_7$O$_{12}$ tentatively evidencing similar behavior [24,28]. Figure 5(b) depicts the thermal evolution of magnetic moments on A' and B sublattices with the B-site moment decomposed into its χ_b and α_b components. In Fig. 5(c), the magnetostrictive β component is superimposed on the squared magnetic moments on each sublattice. The two quantities follow the same trend with temperature and indeed are shown to be proportionate in the inset of the figure. This result implies a linear-quadratic coupling of the lattice to the magnetic order parameter, which is discussed in detail in the following section.
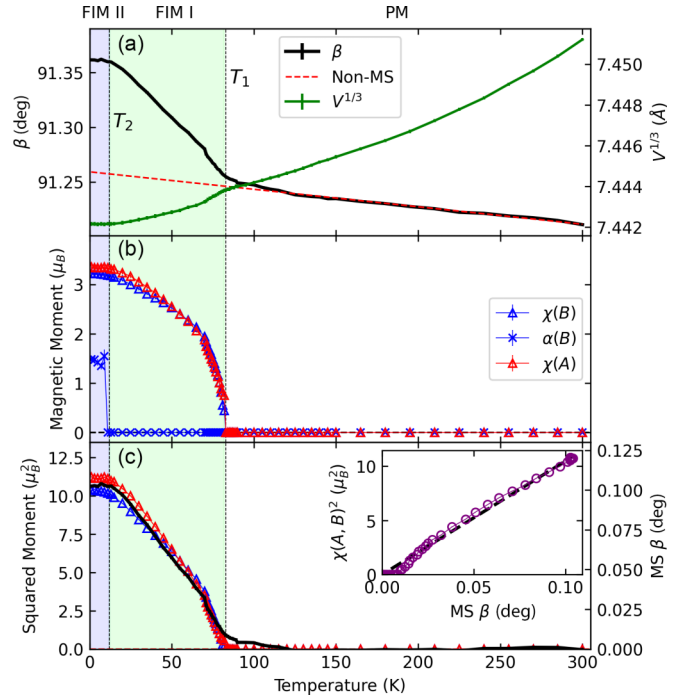

FIG. 5. (a) Distortion of monoclinic β angle (left axis, black) against temperature with the cube-rooted unit cell volume (right axis, green) overlaid. A linear fitting of β against temperature in the paramagnetic phase is depicted in red. The deviation of β from this fit is assumed to be magnetostrictive. (b) Thermal evolution of magnetic moment components on Mn^{3+} sites. Orthogonal B-site components associated with Γ-point (χ) and ICM (α) magnetic order are indicated with triangles and crosses, respectively. (c) Magnetostrictive (MS) change in β (right axis) with the χ-mode moments squared (left axis) overlaid. The inset depicts the average χ-mode moment across A' and B sites squared plotted against the change in β.

IV. DISCUSSION

The results outlined above invite a group-theoretical analysis of the coupling of structural strain or displacive modes to the Γ-point χ_i magnetic modes. Taking the $Im\bar{3}$ QPM aristotype as the parent, monoclinic distortions lowering the crystal symmetry to $I2/m$ transform as the $(0, \delta_b, 0)$ order parameter direction (OPD) of the Γ_4^+ irrep. Among the symmetry-adapted normal modes of this irrep are those associated with cooperative JT distortions akin to those observed in LaMnO$_3$. Indeed, it is the orbital instability of the octahedrally coordinated Mn^{3+} B sites that establish the monoclinic structure at high temperature. Also, transforming by this irrep and OPD is a shear lattice strain described by the infinitesimal strain tensor:

$$\begin{bmatrix} 0 & 0 & e_{xz} \\ 0 & 0 & 0 \\ e_{xz} & 0 & 0 \end{bmatrix}.$$

This lattice strain is precisely that associated with the deviation of β from its cubic value of $90°$. Hence, the anomalous increase in β observed on cooling below T_1 indicates a coupling of $\Gamma_4^+(0, \delta_b, 0)$ structural distortions to the magnetic modes. It should be noted that, for all symmetry-adapted modes of the Γ_4^+ irrep, the special OPD simply determines

TABLE V. Γ-point symmetry-adapted magnetic modes of PrMn$_7$O$_{12}$ with respect to the $Im\bar{3}$ parent. The modes are labeled F and χ, as defined in Tables II and III. Subscripts differentiate between the unique directions of χ and α AFM modes, while superscripts denote the associated moment directions in a Cartesian basis coincident with the parent cubic axes.

Irrep	OPD	A-site modes	B-site modes
$m\Gamma_4^+$	$(\eta_a, 0, 0)$	$F^x, \chi_a^x, \chi_b^x, \chi_c^x$	F^x, χ_c^y, χ_b^z
	$(0, \eta_b, 0)$	$F^y, \chi_a^y, \chi_b^y, \chi_c^y$	F^y, χ_a^z, χ_c^x
	$(0, 0, \eta_c)$	$F^z, \chi_a^z, \chi_b^z, \chi_c^z$	F^z, χ_b^x, χ_a^y

which of the parent basis vectors are established as the unique axis of the $I2/m$ isotropy subgroup, with $(\delta_a, 0, 0)$ establishing **a**, $(0, \delta_b, 0)$ establishing **b**, and $(0, 0, \delta_c)$ establishing **c**. We take **b** to be the unique axis, maintaining convention for the monoclinic cell and ensuring that lattice basis vectors of the parent cell correspond to those of the subgroup.

Of the magnetic modes observed, the FIM I structure transforms as the $(\eta_a, 0, \eta_c)$ OPD of the $m\Gamma_4^+$ magnetic irrep. A summary of the magnetic modes associated with each of the observed irreps is presented in Table V. A systematic search of free-energy invariants coupling the Γ_4^+ structural distortions to the $m\Gamma_4^+$ magnetic modes of the FIM I phase reveals the trilinear invariant:

$$\mathcal{F}(\Gamma_4^+ : m\Gamma_4^+) = \delta_a\eta_b\eta_c + \delta_b\eta_c\eta_a + \delta_c\eta_a\eta_b. \quad (1)$$

Notably, with reference to the magnetic modes in Table V, one can show that the above invariant cannot be mapped onto intrasublattice Heisenberg-like interactions consistent with the empirically determined magnetic structure. Rather, the invariant is mapped onto magnetostrictive Heisenberg-like $A'B$ exchange interactions. For example, the second term relevant to our **b** unique convention maps onto a mean-field exchange energy of the form:

$$E(\Gamma_4^+ : m\Gamma_4^+) \propto (\beta - \beta_0)\left[\chi_a^x(A')\chi_b^x(B) + \chi_a^z(A')\chi_b^z(B)\right], \quad (2)$$

where the bracketed letters indicate the sublattice hosting the magnetic modes and $\beta_0 = 90°$. While other intrasublattice interactions surely exist, the large magnetostrictive distortion nonetheless evidences that strong intersublattice interactions between nearest-neighbor A' and B sites are important in stabilizing the magnetic structure of the FIM I phase.

The wider phase diagram is explored in Appendix B, where a minimal Heisenberg model is developed, heavily constrained to the empirical magnetic structures found across the RMn$_7$O$_{12}$ family. The model, which includes average nearest-neighbor $A'B$ and BB exchange (Fig. 6) and next-nearest-neighbor BB exchange, captures all magnetic structures observed, including canted CM and ICM ground states. It is apparent that no single tuning parameter explains the different phases observed across the rare-earth QPMs. However, our minimal model indicates that the larger rare-earth ions lead to a larger $J_{BB}/J_{A'B}$ ratio, giving rise to spin canting, which are then separated in propagation vectors by J'_{BB}/J_{BB}.
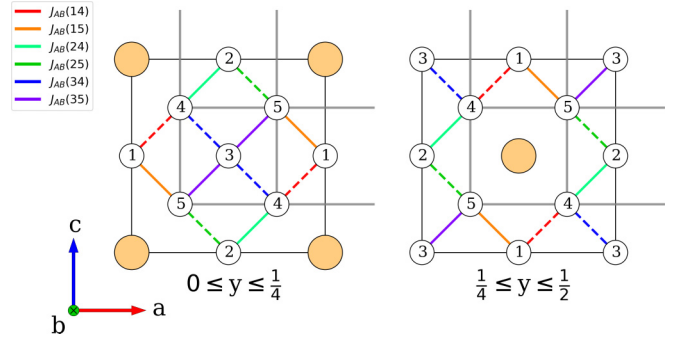

FIG. 6. Exchange interaction pathways viewed down the b axis, for slices through the unit cell $0 \leqslant y \leqslant \frac{1}{4}$ (left) and $\frac{1}{4} \leqslant y \leqslant \frac{1}{2}$ (right). The region $\frac{1}{2} \leqslant y \leqslant 1$ is equivalent by mirror symmetry. All symmetry-inequivalent $A'B$ interactions are colored, with solid and dashed lines set to be ferromagnetic and antiferromagnetic, respectively, in the mean-field calculations. BB interactions are indicated by thick black lines (next-nearest-neighbor BB exchange interactions and BB exchange $\parallel$ b are omitted for clarity), and the unit cell is shown in thin black lines. Transition metal atoms are numbered according to Table II, and Pr atoms are shown as yellow spheres.

V. CONCLUSIONS

In summary, we have solved the magnetic structures of PrMn$_7$O$_{12}$, resolving two distinct magnetic phases. The high-temperature magnetic structure of the FIM I phase resembles those observed in related trivalent-R QPM systems, consisting of FIM order on A$'$ sites and AFM order on B sites. At low temperature, an additional magnetic phase transition occurs to a highly canted FIM II phase, characterized by a superposed ICM modulation of the high-temperature order on B sites, resembling the ground state of NdMn$_7$O$_{12}$. We demonstrate strong magnetoelastic coupling between the symmetry-adapted magnetic modes of the FIM I phase and a sheer lattice strain, which can be understood in terms of a phenomenological model that demonstrates that $A'B$ exchange is primarily responsible for the FIM structures observed across the R^{3+} QPM family. Additionally, an empirically constrained analytical minimal model is formulated and shown to capture all magnetic structures observed, including canted CM and ICM phases.

APPENDIX A: LATTICE PARAMETERS

Figure 7 shows the monoclinic $I2/m$ lattice parameters a, b, and c refined against NPD data measured as a function of temperature. Note that the monoclinic angle β and unit cell volume are shown in Fig. 5.
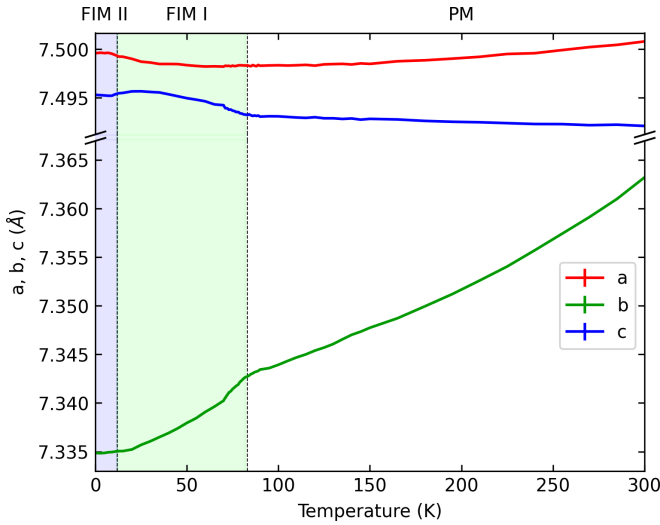
FIG. 7. Temperature dependence of the monoclinic $I2/m$ lattice parameters a, b, and c.

APPENDIX B: MEAN-FIELD HEISENBERG MODEL

It was previously suggested that the second magnetic phase transition found in RMn$_7$O$_{12}$ (R = La and Nd) at T_2 likely originates in the competition between $A'B$ and BB exchange, where $A'B$ interactions were assumed to be large (now confirmed above), while BB exchange is compromised by the large degree of octahedral tilting [24]. It was further assumed that $A'A'$ exchange is negligible. We now test this proposal by developing a minimal mean-field Heisenberg model. We stress that this model is greatly simplified by heavy constraints based upon the observed RMn$_7$O$_{12}$ magnetic structures. As such, it serves only as a proof of principle regarding the stabilization of CM and ICM canted ground states and indicates the hierarchy of exchange interactions, their competition, and tuning between different compositions.

We begin by partitioning the mean-field spin Hamiltonian into a term that stabilizes the Γ-point χ-type magnetic structure on the A' and B sites and a term that stabilizes a $\mathbf{k} = (k, 1, -k)$ α-type magnetic structure on the B sites (note we have set $|k_x| = |k_z|$ for simplicity):

$$\mathcal{H} = \mathcal{H}^{\chi} + \mathcal{H}^{\alpha}, \tag{B1}$$

where

$$\mathcal{H}^{\chi} = -48 J_{A'B} S_{A'}^{\chi} S_B^{\chi} + 24 J_{BB} \left(S_B^{\chi}\right)^2 + 8 J'_{BB} \left(S_B^{\chi}\right)^2, \tag{B2}$$

and

$$\mathcal{H}^{\alpha} = -16 J_{BB} \left(S_B^{\alpha}\right)^2 \cos(\pi k) - 8 J_{BB} \left(S_B^{\alpha}\right)^2$$
$$+ 8 J'_{BB} \left(S_B^{\alpha}\right)^2 \cos(2\pi k), \tag{B3}$$

where $S_{A'}^i$ and S_B^i are the magnetic moment components on the A' and B sublattices, associated with the ith mode ($i = \chi, \alpha$). To make the problem tractable yet informative, we have imposed the following simplifications. The $A'B$ interactions parameterized as $J_{A'B}$ were set to all be equivalent in magnitude and with signs supporting the empirical FIM I
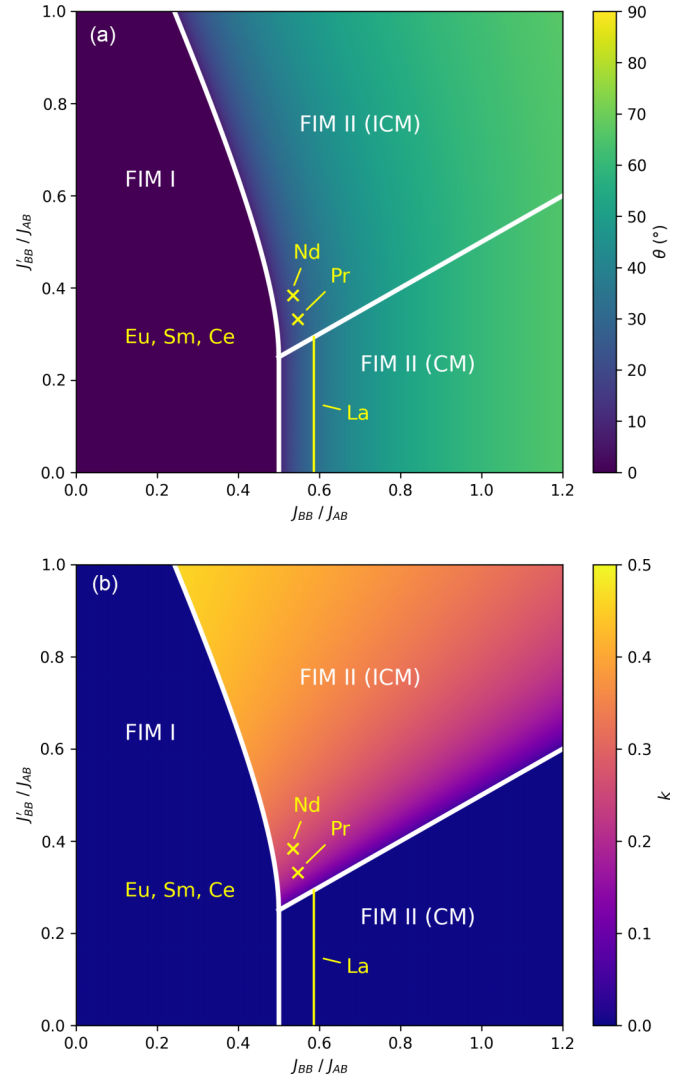

FIG. 8. Phase diagrams in J_{BB} and J'_{BB} depicting (a) the canting angle θ, defined as $\tan(\theta) = \frac{S_B^H}{S_B^\Gamma}$ and (b) component k in propagation vector $(k, 1, -k)$. On both, the positions of R = Nd and Pr systems have been marked using knowledge of their empirically determined canting angles and propagation vectors, while the canting angle of the La system has been used to mark the locus of points it may occupy on the phase diagram. The position of R = Eu, Sm, and Ce systems could not be determined since they adopt pure FIM I ground-state magnetic structure, but given the positions of the other rare-earth ions with similar atomic radii, one can assume they lie in the vicinity of the triple point at $J_{BB} = \frac{1}{2}, J'_{BB} = \frac{1}{4}$.

structure (Fig. 6). Similarly, the nearest-neighbor BB interactions were set to be AFM along $\mathbf{b}$ and FM along $\mathbf{a}$ and $\mathbf{c}$, all equal in magnitude parameterized by J_{BB}. Next-nearest-neighbor BB interactions were implemented along the [0.5, 0, −0.5] directions, parameterized as J'_{BB}, which introduce an instability toward ICM α modes. Similar super-superexchange interactions were found to be significant in the orthorhombic perovskites due to the octahedral tilting distortions bringing two apical oxygen ions close together along this cubic perovskite face diagonal [33]. We impose the constant moment

condition $(S^\chi)^2 + (S^\alpha)^2 = S^2$, giving

$$\mathcal{H} = 8\left(S_B^\chi\right)^2[4J_{BB} + J'_{BB} + J(k)] - 48J_{A'B}S_B^\chi S_{A'}^\chi$$
$$- 8J_{BB}S^2 - 8J(k)S^2, \qquad (B4)$$

where the propagation vector-dependent part is defined as

$$J(k) = 2J_{BB}\cos(\pi k) - J'_{BB}\cos(2\pi k). \qquad (B5)$$

We have assumed that the α mode results in spin canting, which in the ICM case is manifest as an additional helicoidal order with spin components in the plane perpendicular to the χ modes. Trivially, $S^\alpha = 0$ corresponds to the collinear FIM I structure. Differentiating with respect to k, one finds

$$\frac{\partial \mathcal{H}}{\partial k} = 16\pi \sin(\pi k)\left(S^2 - S_B^{\chi\,2}\right)[J_{BB} - 2J'_{BB}\cos(\pi k)], \quad (B6)$$

which gives stationary points at

(1) $S_B^\chi = S$, corresponding to a fully saturated moment and hence zero canting;

(2) $k = 0$, which for $S_B^\chi < S$ corresponds to the CM canted state of LaMn$_7$O$_{12}$;

(3) $\cos(\pi k) = \frac{J_{BB}}{2J_{BB'}}$, which for $S_B^\chi < S$ corresponds to the ICM canted states of NdMn$_7$O$_{12}$ and PrMn$_7$O$_{12}$.

By evaluating the stability of these stationary points with $S_B^\chi < S$, one finds that the phase boundary between the CM and ICM canted phases is defined by

$$\frac{J'_{BB}}{J_{BB}} = \frac{1}{2}. \qquad (B7)$$

Differentiating with respect to S_B^χ, one finds

$$\frac{\partial \mathcal{H}}{\partial S_B^\chi} = 8\left\{2S_B^\chi[4J_{BB} + J'_{BB} + J(k)] - 6J_{A'B}S_{A'}^\chi\right\}, \qquad (B8)$$

which yields a stationary point at

$$\frac{S_B^\chi}{S_{A'}^\chi} = \frac{3J_{A'B}}{[4J_{BB} + J'_{BB} + J(k)]}. \qquad (B9)$$

The observed absence of canting on the A' sites implies $S_{A'}^\chi = S$, and hence, $S_B^\chi/S_{A'}^\chi \leqslant 1$. Equation (B9) then gives

$$4J_{BB} + J'_{BB} + J(k) \leqslant 3J_{A'B}. \qquad (B10)$$

The boundary between the FIM I phase and the canted CM phase can then be obtained by setting $k = 0$ in Eq. (B10):

$$\frac{J_{BB}}{J_{A'B}} = \frac{1}{2}. \qquad (B11)$$

Substituting $\cos(\pi k) = \frac{J_{BB}}{2J_{BB'}}$ into Eq. (B10) yields the boundary between FIM I and the ICM canted phase, which is described by the equation:

$$\frac{J'_{BB}}{J_{A'B}} = \frac{1}{4}\left[\left(3 - 4\frac{J_{BB}}{J_{A'B}}\right)\right.$$
$$\left. + \sqrt{\left(3 - 2\frac{J_{BB}}{J_{A'B}}\right)\left(3 - 6\frac{J_{BB}}{J_{A'B}}\right)}\,\right]. \qquad (B12)$$

The above analytical results are summarized as a phase diagram in Fig. 8. The canting angle generated by orthogonal χ and α components is shaded in the top pane, while the propagation vector component k is shaded in the lower pane. The above phase boundaries are indicated by solid white lines. Using the values of the canting angle and propagation vector, the approximate locations of QPM systems with different rare-earth A-site cations are shown on the diagram. The results suggest that the large rare-earth systems $R =$ Nd, Pr, and La lie within the vicinity of the triple point $J_{BB}/J_{A'B} = \frac{1}{2}$, $J'_{BB}/J_{A'B} = \frac{1}{4}$. The ratio $J_{BB}/J_{A'B}$ must be sufficiently large to produce finite canting, while the CM La system lies below the phase boundary $J'_{BB}/J_{BB} = \frac{1}{2}$, separating it from the ICM ground states of the Nd and Pr systems. The rare-earth cation systems exhibiting only the pure FIM I phase in the ground state, i.e., $R =$ Eu, Sm, and Ce, lie within the leftmost phase for small $J_{BB}/J_{A'B}$. It is apparent that no single tuning parameter explains the different phases observed across the rare-earth QPMs. However, our minimal model indicates that the larger rare-earth ions lead to a larger $J_{BB}/J_{A'B}$ ratio, which are then separated by J'_{BB}/J_{BB}.

[1] J. M. Coey, M. Viret, and S. Von Molnár, Mixed-valence manganites, Adv. Phys. **48**, 167 (1999).

[2] J. B. Goodenough, Theory of the role of covalence in the perovskite-type manganites [La,*M*(II)]MnO$_3$, Phys. Rev. **100**, 564 (1955).

[3] S. Jin, T. H. Tiefel, M. McCormack, R. A. Fastnacht, R. Ramesh, and L. H. Chen, Thousandfold change in resistivity in magnetoresistive La-Ca-Mn-O films, Science **264**, 413 (1994).

[4] T. Kimura, T. Goto, H. Shintani, K. Ishizaka, T. Arima, and Y. Tokura, Magnetic control of ferroelectric polarization, Nature (London) **426**, 55 (2003).

[5] I. Yamada, H. Fujii, A. Takamatsu, H. Ikeno, K. Wada, H. Tsukasaki, S. Kawaguchi, S. Mori, and S. Yagi, Bifunctional oxygen reaction catalysis of quadruple manganese perovskites, Adv. Mater. **29**, 1603004 (2017).

[6] M. B. Hanif, S. Rauf, M. Motola, Z. U. D. Babar, C. J. Li, and C. X. Li, Recent progress of perovskite-based electrolyte materials for solid oxide fuel cells and performance optimizing strategies for energy storage applications, Mater. Res. Bull. **146**, 111612 (2022).

[7] Z. Shi, J. Zhang, J. Wei, X. Hou, S. Cao, S. Tong, S. Liu, X. Li, and Y. Zhang, *A*-site deficiency improved the thermoelectric performance of high-entropy perovskite manganite-based ceramics, J. Mater. Chem. C **10**, 15582 (2022).

[8] A. N. Vasil'ev and O. S. Volkova, New functional materials AC$_3$B$_4$O$_{12}$ (Review), Low Temp. Phys. **33**, 895 (2007).

[9] A. A. Belik, R. D. Johnson, and D. D. Khalyavin, The rich physics of *A*-site-ordered quadruple perovskite manganites AMn$_7$O$_{12}$, Dalton Trans. **50**, 15458 (2021).

[10] A. M. Glazer, The classification of tilted octahedra in perovskites, Acta Cryst. B **28**, 3384 (1972).

[11] M. V. Talanov, Group-theoretical analysis of 1:3 A-site-ordered perovskite formation, Acta Cryst. Sect. A **75**, 379 (2019).

[12] J. Chenavas, F. Sayetat, A. Collomb, J. C. Joubert, and M. Marezio, A perovskite-like compound, Solid State Commun. **16**, 1129 (1975).

[13] S. V. Ovsyannikov, A. M. Abakumov, A. A. Tsirlin, W. Schnelle, R. Egoavil, J. Verbeeck, G. Van Tendeloo, K. V. Glazyrin, M. Hanfland, and L. Dubrovinsky, Perovskite-like Mn$_2$O$_3$: A path to new manganites, Angew. Chem. Int. Ed. **52**, 1494 (2013).

[14] R. D. Johnson, L. C. Chapon, D. D. Khalyavin, P. Manuel, P. G. Radaelli, and C. Martin, Giant improper ferroelectricity in the ferroaxial magnet CaMn$_7$O$_{12}$, Phys. Rev. Lett. **108**, 067201 (2012).

[15] S. V. Streltsov and D. I. Khomskii, Jahn-Teller distortion and charge, orbital, and magnetic order in NaMn$_7$O$_{12}$, Phys. Rev. B **89**, 201115(R) (2014).

[16] A. A. Belik, Y. Matsushita, M. Tanaka, R. D. Johnson, and D. D. Khalyavin, A plethora of structural transitions, distortions and modulations in Cu-doped BiMn$_7$O$_{12}$ quadruple perovskites, J. Mater. Chem. C **9**, 10232 (2021).

[17] A. A. Belik, Y. Matsushita, Y. Kumagai, Y. Katsuya, M. Tanaka, S. Y. Stefanovich, B. I. Lazoryak, F. Oba, and K. Yamaura, Complex structural behavior of BiMn$_7$O$_{12}$ quadruple perovskite, Inorg. Chem. **56**, 12272 (2017).

[18] A. Prodi, E. Gilioli, R. Cabassi, F. Bolzoni, F. Licci, Q. Huang, J. W. Lynn, M. Affronte, A. Gauzzi, and M. Marezio, Magnetic structure of the high-density single-valent e_g Jahn-Teller system LaMn$_7$O$_{12}$, Phys. Rev. B **79**, 085105 (2009).

[19] Z. Popovic and S. Satpathy, Cooperative Jahn-Teller coupling in the manganites, Phys. Rev. Lett. **84**, 1603 (2000).

[20] Y. Murakami, J. P. Hill, D. Gibbs, M. Blume, I. Koyama, M. Tanaka, H. Kawata, T. Arima, Y. Tokura, K. Hirota *et al.*, Resonant x-ray scattering from orbital ordering in LaMnO$_3$, Phys. Rev. Lett. **81**, 582 (1998).

[21] X. Qiu, T. Proffen, J. F. Mitchell, and S. J. L. Billinge, Orbital correlations in the pseudocubic O and rhombohedral R phases of LaMnO$_3$, Phys. Rev. Lett. **94**, 177203 (2005).

[22] J. Kanamori, Superexchange interaction and symmetry properties of electron orbitals, J. Phys. Chem. Solids **10**, 87 (1959).

[23] P. W. Anderson, Antiferromagnetism. Theory of superexchange interaction, Phys. Rev. **79**, 350 (1950).

[24] R. D. Johnson, D. D. Khalyavin, P. Manuel, L. Zhang, K. Yamaura, and A. A. Belik, Magnetic structures of the rare-earth quadruple perovskite manganites RMn$_7$O$_{12}$, Phys. Rev. B **98**, 104423 (2018).

[25] D. Behr, A. A. Belik, D. D. Khalyavin, and R. D. Johnson, BiMn$_7$O$_{12}$: Polar antiferromagnetism by inverse exchange striction, Phys. Rev. B **107**, L140402 (2023).

[26] R. D. Johnson, D. D. Khalyavin, P. Manuel, Y. Katsuya, M. Tanaka, Y. Matsushita, L. Zhang, K. Yamaura, and A. A. Belik, Displacive structural phase transitions and the magnetic ground state of quadruple perovskite YMn$_7$O$_{12}$, Phys. Rev. B **99**, 024107 (2019).

[27] R. D. Johnson, D. D. Khalyavin, P. Manuel, L. Zhang, K. Yamaura, and A. A. Belik, Emergence of a magnetostructural dipolar glass in the quadruple perovskite Dy$_{1-\delta}$Mn$_{7+\delta}$O$_{12}$, Phys. Rev. Lett. **125**, 097601 (2020).

[28] F. Mezzadri, M. Calicchio, E. Gilioli, R. Cabassi, F. Bolzoni, G. Calestani, and F. Bissoli, High-pressure synthesis and characterization of PrMn$_7$O$_{12}$ polymorphs, Phys. Rev. B **79**, 014420 (2009).

[29] L. C. Chapon, P. Manuel, P. G. Radaelli, C. Benson, L. Perrott, S. Ansell, N. J. Rhodes, D. Raspino, D. Duxbury, E. Spill *et al.*, WISH: The new powder and single crystal magnetic diffractometer on the second target station, Neutron News **22**, 22 (2011).

[30] J. Rodríguez-Carvajal, Recent advances in magnetic structure determination by neutron powder diffraction, Phys. B: Condens. Matter **192**, 55 (1993).

[31] B. J. Campbell, H. T. Stokes, D. E. Tanner, and D. M. Hatch, ISODISPLACE: A web-based tool for exploring structural distortions, J. Appl. Cryst. **39**, 607 (2006).

[32] H. T. Stokes, D. M. Hatch, and B. J. Campbell, ISOTROPY software suite, https://iso.byu.edu.

[33] N. S. Fedorova, Y. W. Windsor, C. Findler, M. Ramakrishnan, A. Bortis, L. Rettig, K. Shimamoto, E. M. Bothschafter, M. Porer, V. Esposito *et al.*, Relationship between crystal structure and multiferroic orders in orthorhombic perovskite manganites, Phys. Rev. Mater. **2**, 104414 (2018).